

# An investigation of magnetic field distortions in accretion discs around neutron stars

L. Naso<sup>1</sup> and J.C. Miller<sup>1,2</sup>

<sup>1</sup> SISSA and INFN, via Beirut 2-4, I-34151 Trieste, Italy

<sup>2</sup> Department of Physics (Astrophysics), University of Oxford, Keble Road, Oxford OX1 3RH, UK

## ABSTRACT

We report results from calculations investigating stationary magnetic field configurations in accretion discs around magnetised neutron stars. Our strategy is to start with a very simple model and then progressively improve it providing complementary insight into results obtained with large numerical simulations. In our first model, presented here, we work in the kinetic approximation and consider the stellar magnetic field as being a dipole aligned with the stellar rotation axis and perpendicular to the disc plane, while the flow in the disc is taken to be steady and axisymmetric. The behaviour in the radial direction is then independent of that in the azimuthal direction. We investigate the distortion of the field caused by interaction with the disc matter, working in full 2D and solving the induction equation numerically. The influence of turbulent diffusivity and fluid velocity on the poloidal field configuration is analysed, including discussion of outflows from the top and bottom of the disc. We find that the distortions increase with increasing magnetic Reynolds number  $R_m$  (calculated using the radial velocity). However, a single global parameter does not give an adequate description in different parts of the disc and we use instead a ‘magnetic distortion function’  $D_m(r, \theta)$  (a magnetic Reynolds number defined locally). Where  $D_m \ll 1$  (near to the inner edge of the disc) there is little distortion, but where  $D_m \gg 1$  (most of the rest of the disc), there is considerable distortion and the field becomes weaker than the dipole would have been. Between these two regions, there is a transition zone where the field is amplified and can have a local minimum and maximum. The location of this zone depends sensitively on the diffusivity. The results depend very little on the boundary conditions at the top of the disc.

**Key words.** Accretion, accretion disks – Magnetic fields – Magnetohydrodynamics (MHD) – Turbulence – Methods: numerical – X-rays: binaries

## 1. Introduction

Magnetic fields play a fundamental role in the physics of accretion discs. First of all they are thought to be the origin of the turbulence which makes the accretion itself possible: this turbulence is usually thought to be caused by the magneto-rotational instability MRI (Velikov 1959, Chandrasekhar 1960, Balbus & Hawley 1991) although recently other important instabilities have been suggested that can operate even when MRI cannot (shear-driven instability, Bonanno & Urpin 2006, 2007; current-driven Tayler instability, Tayler 1973, Rüdiger et al. 2007). Secondly they can also determine the geometric and kinetic structure of the disc. In addition, magnetic fields are invoked to explain several characteristic features of accreting systems, such as particle collimation (jets), radiation collimation (pulsar light-house effect) and spectral line production (cyclotron and synchrotron emission). There are hints that magnetic fields are active even in the dead zones of protoplanetary discs where they transfer angular momentum outwards (Turner & Sano 2008). Overall, it seems that regardless of the particular kind of accreting system, from ones around supermassive black holes in the centres of galaxies to ones around protostars in star-forming regions, magnetic fields are almost always present and playing some role. With this paper, we begin a study of the properties of accretion discs around magnetised neutron stars. In particular, we are interested in two kinds of system: X-ray pulsars and old neutron stars in the process of being spun-up (recycled) to become millisecond pulsars (MSPs).

In X-ray pulsars the accreted matter transfers angular momentum to or from the neutron star causing the spin frequency to increase or decrease at rates that are often hundreds of times faster than the typical spin-down rate in radio pulsars. Some of them are observed to be continuously speeding up or slowing down (with occasional reversals in these trends) while others show either little change in period or display erratic spin-down and spin-up behaviour (see, for example, the review by Bildsten et al. 1997). Exactly why the X-ray pulsars show such varied spin behaviour is still not clearly understood, but the magnetic field is almost certainly playing an important role in this. X-ray pulsars typically have magnetic fields of  $\sim 10^{12}$  G and rotation periods in the range  $10^2 - 10^3$  s.

Old pulsars in the process of being recycled have lower magnetic fields (typically  $\sim 10^8$  G) and are being spun up to millisecond periods by means of accretion from their binary companion via an accretion disc. Their relatively weak magnetic fields allow the inner edge of the disc to be close to the surface of the star. There has been recent evidence that the standard evolutionary model cannot explain the evolution of all MSPs, especially the young ones with relatively high magnetic fields, e.g. PSR B1937+21. Kiziltan & Thorsett (2009) showed that different MSPs must form by at least two distinct processes, but the nature of the second process remains unknown.

Here we focus mostly on these “recycled pulsars”, for which the distortions of the magnetic field are larger and occur at smaller distances from the central object, making the effects easier to see. The behaviour for the X-ray pulsars is expected to be mainly similar, although one must then scale quantities because

of the larger inner radius of the disc and intensity of the magnetic field.

One of the first important theoretical studies of accretion onto magnetised neutron stars was made by Ghosh, Lamb & Pethick (1977) who investigated the flow of accreting matter and the magnetic field configuration in the region inside the Alfvén surface (taken to roughly coincide with the magnetospheric boundary). In this pioneering work they were able to estimate the total torque exerted on the neutron star by the accretion disc, but at the cost of making many strong and questionable assumptions. For example, they assumed that the disc is completely screened from the field except in a very small transition region, whereas there are some mechanisms (Kelvin-Helmholtz instability, turbulent diffusion and magnetic field reconnection) that allow the magnetic field to thread the disc across a very large region, as the same authors noted in a subsequent paper Ghosh & Lamb (1979a, hereafter GL). Also, they used an *ad hoc* prescription for the azimuthal field, which was later shown to be inconsistent with having a stable disc beyond the corotation point (Wang 1987). They made a number of other assumptions which, while being approximations, are still used nowadays, such as having axisymmetry, a steady flow, infinite conductivity and a thin disc. The GL model was then used for calculating the torque in Ghosh & Lamb (1979b), where they pointed out that there are both positive and negative contributions to the torque, and that if the star rotates fast enough (with respect to the matter in the disc) the net torque can even be negative.

In considering mechanisms for angular momentum loss from neutron stars, one should recall that there are at least two other processes which may well play a significant role: equatorial ejection of matter from the disc - this is the propeller mechanism (Davidson & Ostriker 1973; Illarionov & Sunyaev 1975; Shakura 1975); and gravitational wave emission, which would occur if the neutron star has some mass (or mass-current) asymmetry around its rotation axis (see Abbott et al. (2007)).

A significant step forward in studying these magnetic torques was made by Wang (1987) and Campbell (1987, 1992), who reconsidered the  $B_\phi$  generation mechanism. They succeeded in obtaining an analytical expression for the azimuthal component of the magnetic field, which is still used despite the simplified nature of the model assumptions (e.g. having an exactly dipolar poloidal field and considering only the equatorial plane). In these models the induction equation is solved so as to find a steady solution for an axisymmetric magnetic field. They found that the generation of toroidal field is due only to the vertical gradient of the azimuthal velocity  $v_\phi$ . If one further assumes that the disc is Keplerian ( $\Omega = \Omega_K$ ) and that the magnetosphere just above the disc is corotating with the star (with angular velocity  $\Omega^*$ ), then one obtains that  $B_\phi \propto \Omega_K - \Omega^*$ . The magnetic torque is then calculated and, depending on the radii of the inner edge of the disc and of the corotation point  $r_c$ , can either spin-up or spin-down the neutron star.

Our aim in the present work is to improve on this analysis and to find a stationary configuration for the magnetic field inside the disc and in the surrounding corona (the latter taken as being a layer above and below the disc), without making any leading order expansion or vertical integration, i.e. using a fully 2D model. We want to study the effects of the relevant physical quantities (the radial, vertical and angular velocities, the diffusivity, the accretion rate, etc.) on the structure of the magnetic field, and in turn on the magnetic torque, in order to give an estimate for the field structure in the disc which is more realistic than the analytic ones given by Wang (1987) and Campbell (1987, 1992). We start by making use of the kinematic approximation (i.e. we

consider the induction equation for a given profile of fluid quantities and do not solve the Euler equation to incorporate back reaction on the fluid from the field). Subsequently one can refine this model by including other important aspects, such as magnetic back reaction.

Miller & Stone (1997) used a 2D model, including the effects of non-zero resistivity in the MHD equations. They considered the time evolution of an initial magnetic field profile but did not follow the evolution for long enough to reach a steady state. They found that regardless of the initial field structure (they used 3 configurations) there was a rapid evolution of the disc, driven by angular momentum transport. In most cases, equatorial accretion results, either because accumulation of matter makes the gas pressure exceed the magnetic pressure or because the magnetic field geometry is such that polar accretion is inhibited. Polar accretion only occurs when a strong global vertical magnetic field is included. Their simulations also confirmed the failure of total screening of the magnetic field from the accretion disc.

Many investigators after Miller & Stone have simulated the magnetosphere-disc interaction, solving the full set of the MHD equations (see e.g. Romanova et al 2002 and Kulkarni & Romanova 2008). The work that we are carrying out here should not be seen as being in competition with these analyses, but rather as being complementary to them. Our approach here is to use a succession of simplified models, becoming progressively more sophisticated, and to proceed step by step so as to fully understand the effect of each successive additional feature as it is introduced. In large-scale numerical work, one sees the results of an interacting set of inputs within the scope of the adopted model assumptions and numerical techniques. Deconstructing this, so as to have a clear conceptual understanding of the role of each of the different components, remains a valuable thing to do and an approach which needs to be carried on alongside the large-scale simulations. The conceptual papers from the 1970s and 1980s, mentioned above, continue to be widely quoted and used as the basis for new research (see, for example, Kluzniak & Rappaport 2007) and our work here stands in the tradition of refining these approaches.

Agapitou & Papaloizou (2000) looked for steady-state axisymmetric configurations of a force-free magnetosphere using simplified numerical calculations. However they focused on the global structure of the whole magnetosphere, rather on the details of what happens inside the disc. Moreover in their model the disc is assumed to have only an azimuthal velocity and to be thin so that radial derivatives can be neglected with respect to vertical ones. They found that even under these circumstances the poloidal field can differ significantly from the dipole field of the central star, and that the magnetic torque can be much smaller than that estimated assuming  $B_z \sim B_{\text{dip}}$ .

Following a somewhat similar strategy, we aim to make improved calculations by using a more general profile of the velocity field (with all of the components being allowed to be non-zero); by not neglecting any of the derivatives present in the induction equation; and by using a better resolution (i.e. a finer grid) and a much larger numerical domain in the radial direction so as not to have the results being dependent on the outer boundary conditions.

The plan of this paper is as follows. After the present Introduction, the details of the model adopted here are given in Section 2, while the equations solved are presented in Section 3. As we will show there, since the system is taken to be axisymmetric and in a stationary state, the induction equation can be split into two parts, one in which only the poloidal component of the magnetic field appears and the other containing all of

the components. In this paper we present results for the poloidal field; the toroidal one will be discussed in a subsequent paper. The numerical code used is described briefly in Section 3, and then in more detail in the Appendix, where we describe both the algorithm used and the tests which we have performed for verifying it. In Section 4 we present our results and Section 5 contains conclusions.

## 2. Our Model

In this study we consider disc accretion by a neutron star having a dipolar magnetic field with magnetic moment  $\mu$ . We assume that the star is rotating around its magnetic axis, and that this axis is perpendicular to the disc plane; also, we assume that the fluid flow is steady and has axial symmetry everywhere. Of course, all pulsars must be oblique rotators in order to be observed as such, and so the system would not then be axisymmetric as a matter of principle. However we are not concerned here with studying the aspects of accreting systems affected by the inclination angle (e.g. the impact region or stellar precession) and the principles of the interaction between the magnetic field and the plasma in the disc are not affected by the inclination. Therefore we feel that retaining the assumption of the magnetic axis being perpendicular to the disc is satisfactory for our purposes. For our calculations, we use spherical coordinates  $(r, \theta, \phi)$ , with the origin being at the centre of the neutron star.

The general flavour of our model is similar to the GL one. We suppose that at large radii the magnetic pressure is negligible with respect to the gas pressure and the disc can be described as a standard  $\alpha$ -disc. As one moves inwards however the magnetic field becomes progressively stronger, and may eventually dominate over the gas pressure so that most of the matter leaves the disc following magnetic field lines and the disc is disrupted. We note that some equatorial accretion continues to be possible even with a rather high stellar magnetic field, as shown by Miller & Stone (1997).

There are some differences between our model and that of GL. We are not assuming the existence of a wide transition zone where the field is progressively screened, eventually disappearing at the outer boundary of the zone. Also, we do not force the field to be zero at the outer boundary; we instead take it to be dipolar there and we do the same at all of the other boundaries as well. We put the radial outer boundary very far away so that the solutions in the zone of interest, which goes from the inner edge of the disc out to the light cylinder, will not be very sensitive to the conditions at the outer edge. We note here that, if we take the innermost part of the disc to have very high diffusivity, we naturally find a narrow inner region followed by a broad outer one, however the behaviour of the field in these regions is quite different from that in the GL model, as will be shown in the results section.

As regards the inner edge of the disc, its precise location is still an open issue and several prescriptions have been suggested, however none of them differs very much from the Alfvén radius calculated using a dipolar magnetic field (i.e. the radius where the pressure of the dipole field equals the gas pressure). For our present model we take this as giving the inner edge of the disc; for subsequent models, a possible improvement will be to calculate the Alfvén radius using the stationary magnetic field obtained in this work instead of the dipolar one.

We suppose that all around the pulsar there is vacuum, except for where we have the disc and the corona, and that the field remains dipolar from the surface of the star until it reaches

the matter in the corona. In reality, taking vacuum is not completely correct, both because the density in the magnetosphere is not zero and because between the star and the disc there is the matter which is accreting onto the neutron star. For the latter, we suppose that the flow of this material is perfectly aligned with field lines and that it has very low density, so that we can neglect its influence on the magnetic field structure. Furthermore we are introducing a low density corona in order to have a transition zone between the disc and the vacuum. We also allow the velocity and the diffusivity to have different values in the corona from those in the disc (we will comment on this later in the present Section).

Summarizing, we model the system as being composed of 4 regions (see figure 1): (1) a central object, surrounded by (2) an accretion disc, on top of which there is (3) a corona; all of the rest is taken to be (4) vacuum. Each physical quantity is allowed to have different values in each of the regions. Our numerical domain covers regions (2) and (3). Since these two regions are surrounded by vacuum and the stellar field is dipolar, we impose dipole boundary conditions at all of the boundaries. We are aware that in real astrophysical systems this dipole condition at the boundaries can be rather drastic since the region outside the neutron star is not vacuum and the field is distorted well before reaching the disc. However at our level of analysis the results are not very sensitively dependent on the precise profile chosen for the magnetic field at the boundaries, and we are here focusing on studying the influence on the magnetic configuration of the velocity field and diffusivity. That this is reasonable is confirmed by the fact that the magnetic configuration which we obtain is rather similar to that given by the numerical simulations of other authors (Miller & Stone, 1997), which had a different treatment of the boundary conditions. We will comment more on this in Section 4.

We take the ratio  $H/r$  to be constant (where  $H$  is the semi-thickness of the disc), and so the entire upper surface of the disc is located at a single value of the colatitude  $\theta$  (as also is the case for the corona). In particular, we take an opening angle of  $8^\circ$  for the disc (measuring from the equatorial plane to the top of the disc), implying  $H/r \sim 0.14$ , and of  $10^\circ$  for the disc plus the corona.

As will be described in Section 3, in this paper we consider only the poloidal component of the induction equation. Once the magnetic diffusivity  $\eta$  and the poloidal velocity  $\mathbf{v}_p$  are specified, this can be solved to obtain the configuration of the poloidal field without entering into details of the toroidal component. As regards the turbulent magnetic diffusivity, we take this to have a constant value  $\eta_0$  in the main disc region and to be  $\eta_c = 100 \cdot \eta_0$  in the corona and in the inner part of the disc (we join the different parts smoothly, using error functions). We take higher values in the latter regions because the density is lower there and so we expect the effects of turbulence to be enhanced. However as we move away from the corona into the vacuum the density drops to zero and turbulence eventually disappears<sup>1</sup>.

As regards the velocity: for  $v_r$  we use the expression given for the middle region of  $\alpha$ -discs<sup>2</sup> by Shakura & Sunyaev (1973); while we put  $v_\theta$  to zero inside the disc, although allowing it to be non-zero in the corona as necessary in order to be consistent with the dipole boundary conditions. In Section 3.2, we find that

<sup>1</sup> It is only the turbulent diffusivity  $\eta_T$  which disappears, the Ohmic one  $\eta_{\text{Ohm}}$  will always be present, therefore in vacuum  $\eta = \eta_{\text{Ohm}} \ll \eta_T$ .

<sup>2</sup> For the parameter values which we are using, both the inner edge of the disc and the outer boundary of our domain of interest lie within the “middle region” of the  $\alpha$ -disc model.

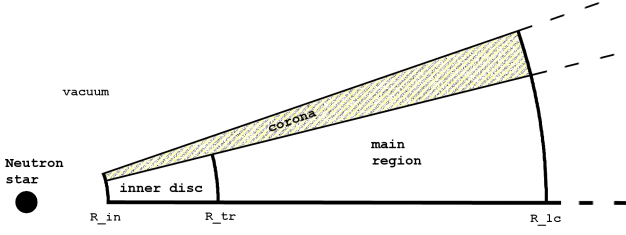


**Fig. 1.** Geometrical representation of our model (the drawing is not to scale). The radius values which we use were:  $R_{in} \sim 10 r_g$ ,  $R_{tr} \sim 22 r_g$  and  $R_{lc} \sim 115 r_g$  and the opening angles are  $8^\circ$  for the disc alone and  $10^\circ$  for disc plus corona. The numerical outer boundary is much further out than the region of interest shown here; the grid continues until  $r \sim 750 r_g$  (this is the reason for the dashed lines).

whenever a dipole field is a solution of the induction equation, a precise relationship must hold between  $v_r$  and  $v_\theta$ , subject to certain reasonable conditions. We use this relation to calculate  $v_\theta$  in the corona.

Figure 1 shows a schematic representation of the geometry of our model: the corona and the two parts of the disc being shown (the transition region is thin and around  $r = R_{tr}$ ). The dashed lines indicate that in solving the induction equation we use a much larger numerical domain, so that in the zone of interest the solution is almost independent of the location of the outer boundary.

### 3. The Equations

The induction equation relates the time variation of the magnetic field to the properties of the plasma. If one considers mean fields, it can be written as:

$$\partial_t \mathbf{B} = \nabla \times (\mathbf{v} \times \mathbf{B} + \mathcal{E} - \eta_{Ohm} \nabla \times \mathbf{B}) \quad (1)$$

where  $\eta_{Ohm} = c^2/4\pi\sigma$  is the Ohmic diffusivity and  $\mathcal{E}$  is the turbulent electromotive force,  $\mathcal{E} \equiv \langle \mathbf{v}' \times \mathbf{B}' \rangle$ , with the primes denoting small-scale turbulent quantities. A common procedure is to expand  $\mathcal{E}$  in terms of the mean field and its derivatives and within the first order smoothing approximation one has  $\mathcal{E} = \alpha \mathbf{B} - \eta_T \nabla \times \mathbf{B}$ , where the  $\alpha \mathbf{B}$  term generates the so-called  $\alpha$ -effect that is fundamental for having a dynamo action. In the present paper we neglect this effect, which could however be included in a more elaborate subsequent model. This is in line with our approach, which is aiming at understanding, one at a time, the effects of the various elements which characterize the system of an accretion disc around a magnetised neutron star.

The induction equation then reduces to:

$$\partial_t \mathbf{B} = \nabla \times (\mathbf{v} \times \mathbf{B} - \eta \nabla \times \mathbf{B}) \quad (2)$$

where  $\eta = \eta_{Ohm} + \eta_T \sim \eta_T$ , because the turbulent diffusivity is much larger than the Ohmic one in the disc and in the corona.

Since we are interested in stationary solutions, we put the time derivatives to zero, as we do also for the  $\phi$  derivatives since we are assuming axisymmetry. Then in spherical coordinates the three components of equation (2) are:

$$0 = \partial_\theta \left\{ \sin \theta \left[ v_r B_\theta - v_\theta B_r - \frac{\eta}{r} [\partial_r(r B_\theta) - \partial_\theta B_r] \right] \right\} \quad (3)$$

$$0 = \partial_r \left\{ r \left[ v_r B_\theta - v_\theta B_r - \frac{\eta}{r} [\partial_r(r B_\theta) - \partial_\theta B_r] \right] \right\} \quad (4)$$

$$0 = \partial_r \left\{ r \left[ v_\phi B_r - v_r B_\phi + \frac{\eta}{r} \partial_r(r B_\phi) \right] \right\} - \partial_\theta \left\{ v_\theta B_\phi - v_\phi B_\theta - \frac{\eta}{r \sin \theta} \partial_\theta(B_\phi \sin \theta) \right\} \quad (5)$$

The first two of these equations have the same expression inside the large square brackets and we call this  $\mathcal{F}$ . We can then reduce these two equations to a single equation and write the entire system as:

$$\mathcal{F} = \frac{k}{r \sin \theta} \quad (6)$$

$$0 = \partial_r \left\{ r \left[ v_\phi B_r - v_r B_\phi + \frac{\eta}{r} \partial_r(r B_\phi) \right] \right\} - \partial_\theta \left\{ v_\theta B_\phi - v_\phi B_\theta - \frac{\eta}{r \sin \theta} \partial_\theta(B_\phi \sin \theta) \right\} \quad (7)$$

where  $k$  is a generic constant.

We notice that  $\mathcal{F}$  depends only on the turbulent magnetic diffusivity  $\eta$  and on the poloidal components of the velocity field and  $r$  and  $\theta$  component of the magnetic field. It is clear therefore that equation (6) alone governs the poloidal part of the magnetic field and is independent of any azimuthal quantity, while to obtain the toroidal component of the magnetic field one has to solve the further equation (7).

In this paper we concentrate only on solving for the poloidal field, using equation (6), for which no knowledge of behaviour in the  $\phi$  direction is required. In a forthcoming paper we will use the results obtained here to solve equation (7) and calculate the toroidal field component.

In order to guarantee that the condition  $\nabla \cdot \mathbf{B} = 0$  is satisfied and to be able to calculate the magnetic field lines easily, we write the magnetic field components in terms of the magnetic stream function  $\mathcal{S}$ , which is implicitly defined by the following two equations:

$$B_r = \frac{1}{r^2 \sin \theta} \partial_\theta \mathcal{S}(r, \theta) \quad (8)$$

$$B_\theta = -\frac{1}{r \sin \theta} \partial_r \mathcal{S}(r, \theta) \quad (9)$$

With this definition, the axisymmetric field  $\mathbf{B}$  is always solenoidal and isolines of  $\mathcal{S}$  represent magnetic field lines. Substituting these expressions into equation (6), we obtain an elliptic partial differential equation (PDE) for  $\mathcal{S}$  in terms of  $r$  and  $\theta$ :

$$\partial_r^2 \mathcal{S} + \frac{1}{r^2} \partial_\theta^2 \mathcal{S} - \left( \frac{\cot \theta}{r^2} + \frac{v_\theta}{r \eta} \right) \partial_\theta \mathcal{S} - \frac{v_r}{\eta} \partial_r \mathcal{S} = \frac{k}{\eta} \quad (10)$$

where  $k$  is the constant introduced in equation (6) and  $v_r$ ,  $v_\theta$  and  $\eta$  are non-constant coefficients. This equation can be solved once boundary conditions and values for the coefficients have been specified.

#### 3.1. Velocity field and turbulent diffusivity

In Section 2 we qualitatively described the profiles of velocity and diffusivity that we are using. Here we give the precise expressions.

For the velocity, we use the expression given by Shakura & Sunyaev (1973):

$$v_r(r) = 2 \cdot 10^6 \cdot \alpha^{4/5} \cdot \dot{m}^{2/5} \cdot m^{-1/5} \cdot (3/r)^{2/5} \left[ 1 - (3/r)^{0.5} \right]^{-3/5} \text{ cm s}^{-1} \quad (11)$$

where the radius  $r$  is expressed in units of the Schwarzschild radius,  $m$  is given in solar mass units,  $\dot{m}$  is in units of the critical

Eddington rate and  $\alpha$  is the standard Shakura-Sunyaev viscosity coefficient. Using typical values ( $\alpha = 0.1$ ,  $\dot{m} = 0.03$  and  $m = 1.4$ ) one obtains:

$$v_r(r) \approx 7.3 \cdot 10^4 \cdot (3/r)^{2/5} \left[1 - (3/r)^{0.5}\right]^{-3/5} \text{ cm s}^{-1} \quad (12)$$

For the other component of the poloidal velocity,  $v_\theta$ , we set this to zero in the disc and use a non-zero profile in the corona. The formula for this is calculated in Subsection 3.2; we anticipate here the result:

$$v_\theta = \begin{cases} 0 & \text{in the disc} \\ \frac{1}{2} v_r \tan \theta & \text{in the corona} \end{cases} \quad (13)$$

For the diffusivity, we first construct two auxiliary functions,  $\eta_\theta$  and  $\eta_r$ , giving the profiles along the  $\theta$  and  $r$  directions respectively:

$$\eta_\theta = \left[1 + \operatorname{erf}\left(\frac{-\theta + \theta_c}{d_\theta}\right)\right] \quad (14)$$

$$\eta_r = \left[1 + \operatorname{erf}\left(\frac{-r + r_{\eta\text{in}}}{d_r}\right)\right] + \left[1 + \operatorname{erf}\left(\frac{r - r_{\eta\text{out}}}{d_r}\right)\right] \quad (15)$$

where  $\theta_c$  is the colatitude of the upper surface of the disc,  $r_{\eta\text{in}}$  is the radius of the boundary between the inner region and the main disc region<sup>3</sup> and  $d_\theta$  and  $d_r$  are the widths of the error functions used for the angular and radial profiles respectively. We then combine equations (14) and (15) to get the global  $\eta$ :

$$\eta(r, \theta) = \eta_0 \cdot \left[1 + \frac{1}{2} \cdot (\eta_\theta + \eta_r) \cdot \left(\frac{\eta_c}{\eta_0} - 1\right)\right] \quad (16)$$

where  $\eta_0$  and  $\eta_c$  are dimensional quantities (with units of  $\text{cm}^2 \text{s}^{-1}$ ), the former giving the value of the diffusivity in the main disc region and the latter giving the value in the corona and the inner disc region.

### 3.2. Dipolar solution, an analytic constraint

In order to obtain a profile for  $v_\theta$  we consider the situation when, from the top surface of the corona (at  $\theta = \theta_{\text{surf}}$ ) down to some  $\theta = \tilde{\theta}$ , the stationary magnetic field is dipolar, i.e.  $(B_r, B_\theta, B_\phi) = \left(\frac{2\mu \cos \theta}{r^3}, \frac{\mu \sin \theta}{r^3}, 0\right)$  where  $\mu$  is the magnetic dipole moment. Since a magnetic dipole field is current-free (i.e.  $\mathbf{J} = \nabla \times \mathbf{B} = 0$ ) equation (2) becomes:

$$\nabla \times (\mathbf{v} \times \mathbf{B}) = 0 \quad (17)$$

Following a procedure similar to that used for obtaining equations (6) and (7), we go to spherical coordinates, write out the three component equations and group the poloidal terms. This gives:

$$v_r B_\theta - v_\theta B_r = \frac{\tilde{k}}{r \sin \theta} \quad (18)$$

$$\partial_r(r v_\phi B_r) = -\partial_\theta(v_\phi B_\theta) \quad (19)$$

where  $\tilde{k}$  is a generic constant. In order to calculate it we consider a path with constant  $\theta$ , e.g.  $\theta = \theta^* \in [\theta_{\text{surf}}, \tilde{\theta}]$ ; along this path equation (18) gives:

$$v_r \left(\frac{\mu \sin \theta^*}{2}\right) - v_\theta (\mu \cos \theta^*) = r^2 \left(\frac{\tilde{k}}{\sin \theta^*}\right) \quad (20)$$

<sup>3</sup>  $r_{\eta\text{out}}$  appearing in the expression for  $\eta_r$  is located shortly before  $r_{\text{out}}$  and far away from the zone of interest.

where all of the terms in the brackets are constant. To investigate further the properties of this equation, consider the situation if  $v_\theta = 0$ . Equation (20) would then imply that either  $v_r \propto r^2$  (which is not reasonable for an accretion flow) or  $v_r = 0$  so that there is no accretion at all. This implies that if we have an accreting flow in a region with a dipole magnetic field then  $v_\theta$  must be non zero. We do not know the exact profiles of  $v_r$  and  $v_\theta$ , but it is not plausible that the left hand side increases as  $r^2$  and so we need to choose  $\tilde{k} = 0$ . Therefore from the last equation we get:

$$v_r \frac{\sin \theta}{2} = v_\theta \cos \theta \rightarrow v_\theta = \frac{1}{2} \tan \theta v_r \quad (21)$$

Equation (21) implies not only that if there is a non-zero radial velocity then there must be a non-zero vertical velocity as well, but also that the vertical velocity is larger than the radial one (for  $\theta = 81^\circ$  one has  $v_\theta \sim 13 v_r$ ).

The behaviour of the azimuthal velocity  $v_\phi$  can be investigated using equation (19). As expected  $v_\phi = 0$  is a possible solution but  $v_\phi = v_{\text{Kep}}$  is not, meaning that having a dipolar field is not consistent with having a Keplerian angular velocity profile, whereas it is consistent with having no rotation. It is interesting to notice that there are also some non trivial profiles which are solutions. For example  $v_\phi \propto r^{-\delta} \cdot \sin^{3+2\delta} \theta$ , where  $\delta$  is a positive integer, gives a set of possible solutions<sup>4</sup>. Therefore if one supposes that  $v_\phi$  decreases with  $r$  as a power law, then it must have also a dependence on  $\theta$  in order for the magnetic field to be dipolar. We recall that in the works of Campbell and Wang it is precisely the vertical gradient of the angular velocity that produces the toroidal field. Here we have shown that it is possible to have a non-zero vertical gradient of the angular velocity and still have a zero toroidal magnetic field. However, we stress that we are not giving physical explanations for having these kinds of velocity profiles.

We note that equation (17) has been solved in the context of stellar winds by Mestel (1961); his result was that the poloidal magnetic field and velocity field need to be parallel. Our result that  $v_r/B_r = v_\theta/B_\theta$  (from equation (18) with  $\tilde{k} = 0$ ) is in agreement with this.

### 3.3. Solution method

Before solving equation (10) we put it into a dimensionless form, by scaling the quantities in the following way:

$$r = \hat{r} r_g \quad \theta = \hat{\theta} \quad S = \hat{S} S_0 \quad (22)$$

where the hat quantities are dimensionless,  $r_g$  is the Schwarzschild radius,  $\eta_0$  is the value of the diffusivity in the main disc region and  $S_0$  is a reference value for the stream function, calculated as the value for a dipolar field on the equator of the neutron star. Substituting into equation (10) we get:

$$\frac{S_0}{r_g^2} \partial_{\hat{r}}^2 \hat{S} + \frac{S_0}{r_g^2 \hat{r}^2} \partial_{\hat{\theta}}^2 \hat{S} - \left(\frac{\cot \hat{\theta}}{r_g^2 \hat{r}^2} + \frac{v_\theta}{r_g \hat{r} \eta}\right) S_0 \partial_{\hat{\theta}} \hat{S} - \frac{v_r}{\eta} \frac{S_0}{r_g} \partial_{\hat{r}} \hat{S} = 0 \quad (23)$$

$$\partial_{\hat{r}}^2 \hat{S} + \frac{1}{\hat{r}^2} \partial_{\hat{\theta}}^2 \hat{S} - \left(\frac{\cot \hat{\theta}}{\hat{r}^2} + \frac{v_\theta r_g}{\hat{r} \eta}\right) \partial_{\hat{\theta}} \hat{S} - \frac{v_r r_g}{\eta} \partial_{\hat{r}} \hat{S} = 0 \quad (24)$$

where we go from (23) to (24) by dividing both sides by  $S_0/r_g^2$ . We rename the variables ( $\hat{r} = x$  and  $\hat{\theta} = y$ ) and obtain the following dimensionless form for the equation:

$$\partial_x^2 \hat{S} + \frac{1}{x^2} \partial_y^2 \hat{S} - \left(\frac{\cot y}{x^2} + \frac{v_\theta r_g}{x \eta}\right) \partial_y \hat{S} - \frac{v_r r_g}{\eta} \partial_x \hat{S} = 0 \quad (25)$$

<sup>4</sup> This can be seen by writing  $v_\phi$  as the product of a function of  $r$  and a function of  $\theta$  and carrying out some simple algebra.

where  $[v_r] = [v_\theta] = \text{cm s}^{-1}$ ,  $[r_g] = \text{cm}$ ,  $[\eta] = \text{cm}^2 \text{s}^{-1}$ , so that  $v_r r_g / \eta$  and  $v_\theta r_g / \eta$  are dimensionless coefficients.

As mentioned above, the reference value for the stream function is taken to be its value at the equator of the neutron star. If we call the star's radius  $\hat{r}_0 r_g$  then  $\mathcal{S}_0 \equiv \mathcal{S}^{\text{dip}}(\hat{r}_0 r_g, \pi/2) = \mu(\hat{r}_0 r_g)^{-1}$ . The solution of equation (25) gives the dimensionless stream function  $\hat{\mathcal{S}}$ . In order to calculate the magnetic field, we first calculate  $\hat{B}_{\text{pol}}$  using the dimensionless versions of equations (8) and (9), and then multiply by  $B_0$  to go to physical units, where  $B_0 \equiv B_\theta^{\text{dip}}(r = \hat{r}_0 r_g, \theta = \pi/2)$ .

We have solved equation (25) with the Gauss-Seidel relaxation method, which uses a finite difference technique, approximating the operators by discretizing the functions over a grid. The value of the stream function at any given iteration step is written as a function of its value at the previous step, or at the same step but at a location which has already been calculated. Details of the numerical scheme are given in the Appendix.

Before applying the numerical scheme to the real problem that we want to solve, we performed a series of tests on the code, which are described in detail in the Appendix. We used several configurations, with many different numbers of grid points, profiles for the velocity and diffusivity, initial estimates for the stream function, locations for the outer radial boundary of the grid and values for the iteration time step. In this way we have checked the stability and convergence, have optimized the iteration procedure and have determined where to place the outer radial boundary of the grid (which needs to be far enough away so that the outer boundary conditions do not significantly influence the solution in our region of interest).

All of the results presented in the next section have been obtained using a  $1000 \times 20$  grid and with  $2^{24} \sim 1.7 \cdot 10^7$  total iterations. With these settings, we have always obtained residuals of the order of  $10^{-14}$  or less, and the resolution is  $\Delta x \sim 0.7 r_g$  and  $\Delta \theta \sim 0.5^\circ$ .

#### 4. Results

From equation (25), we see that in order to calculate the stream function  $\mathcal{S}$ , and hence the poloidal magnetic field, we have to specify  $v_r(r, \theta)$ ,  $v_\theta(r, \theta)$  and  $\eta(r, \theta)$ . For the vertical velocity we follow the prescription given by equation (21); the profiles used for the other two functions have been described previously (see equation (11) for  $v_r$  and Section 2 for  $\eta$ ). Here we describe how the magnetic field configuration changes when we modify these two functions.

In figures 2 and 3 we show the magnetic field lines calculated with four values of  $v_0$ , i.e. with different accretion rates<sup>5</sup>. For facilitating the comparison we show also a dipolar magnetic field (dotted). The field lines are labelled with the radial coordinate where the dipole field imposed at the top boundary would cross the equatorial plane if not distorted. We can see that if  $v_r$  were zero, the field would not be distorted at all from the dipolar configuration and increasing the velocity then creates progressively more distortion. The degree of distortion depends on the location in the disc: in the inner part, where the field is strongest, it is most able to resist distortion; further out, the field is weaker and it becomes progressively more distorted. From the top panel of figure 3 we can see that the distortion increases with distance. For example if one considers only the configuration with  $v_0 = 10^4$ , then one sees that the distortion on the equatorial plane at  $r = 15 r_g$

<sup>5</sup> For the Shakura-Sunyaev model, the radial velocity is proportional to  $\dot{m}^{2/5}$  if the mass of the central object and the viscosity  $\alpha$  are kept fixed.

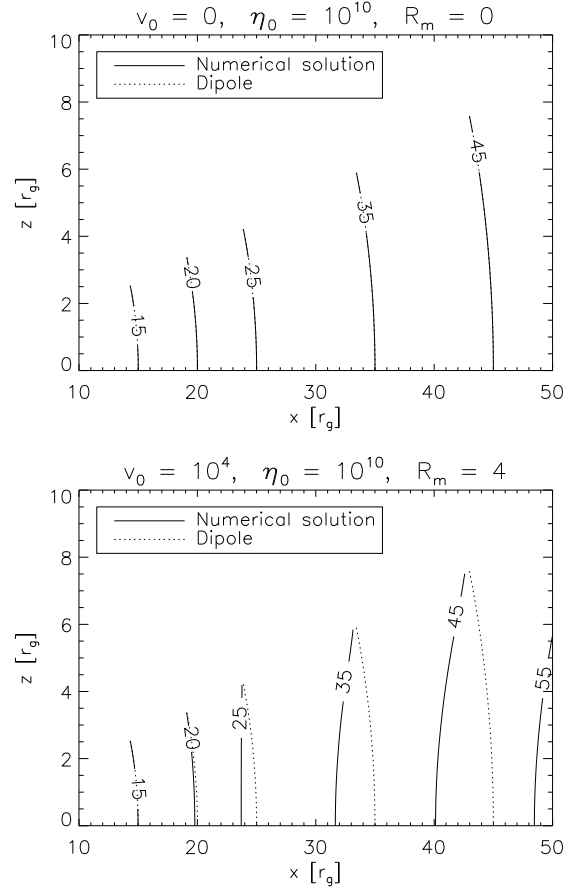


**Fig. 2.** Magnetic field lines from the numerical solution (solid) and those for a dipole (dotted) for comparison. The top panel refers to a case with no accretion, where the field remains exactly dipolar, while in the bottom panel  $v_0 = 10^4 \text{ cm s}^{-1}$ , and the field is distorted. The diffusivity  $\eta_0$  has the same value in both panels ( $10^{10} \text{ cm}^2 \text{s}^{-1}$ ). If we use  $\eta_0 = 10^{11} \text{ cm}^2 \text{s}^{-1}$  and  $v_0 = 10^5 \text{ cm s}^{-1}$ , we obtain the same result as shown in the bottom panel ( $R_m = 4$  for both).

is roughly zero, at  $r = 25 r_g$  it is slightly larger than  $1 r_g$  and at  $r = 45 r_g$  it is about  $5 r_g$ .

According to the behaviour of the magnetic field lines, we can divide the disc into three regions: (1) an inner region, where the lines are not distorted very much away from the dipole; (2) a main region, where the distortion is very large and (3) the region in-between the two, which we call a transition region, where there is an accumulation of field lines. This means that in the transition region there is an amplification of the magnetic field (see figure 4).

In addition to varying the radial velocity, we also consider the role of the diffusivity. The results show that when we change  $\eta_0$ , we get the opposite behaviour to that seen when varying the velocity, i.e. a larger  $\eta_0$  gives a smaller distortion. Actually what really matters is not the velocity or the diffusivity alone but their ratio. This is not surprising since in the equation which we are solving (equation (25)) the quantities only appear in this ratio (bearing in mind that  $v_\theta$  is taken to be either zero or proportional to  $v_r$ ). In fact the magnetic Reynolds number  $R_m$ , which describes the general solution of the induction equation (2), is built from them: it is defined as  $R_m \equiv l_0 \cdot v_0 / \eta_0$ , where  $l_0$ ,  $v_0$

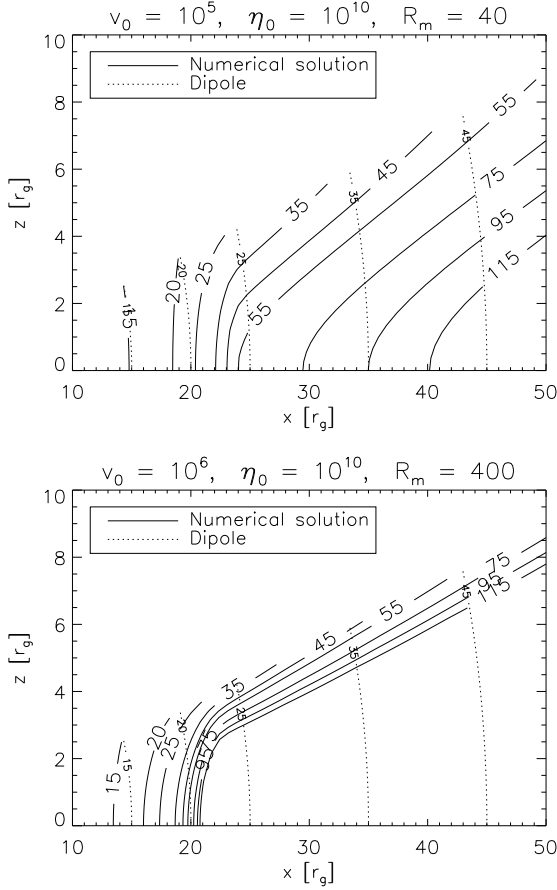


**Fig. 3.** The same as in figure 2, but with different values of  $v_0$ . The top panel is for a case with  $v_0 = 10^5 \text{ cm s}^{-1}$  while the bottom one is for  $v_0 = 10^6 \text{ cm s}^{-1}$ . If we use  $\eta_0 = 10^9 \text{ cm}^2 \text{ s}^{-1}$  and  $v_0 = 10^5 \text{ cm s}^{-1}$ , we obtain the same as in the bottom panel ( $R_m = 400$  for both).

and  $\eta_0$  are respectively a characteristic length, velocity and diffusivity. This parameter gives the relative importance of the two terms on the right-hand side of the induction equation. For large  $R_m$ , we are in the regime of ideal MHD with the magnetic field and plasma being frozen together, for low  $R_m$ , instead, the field and plasma are almost decoupled and the field simply diffuses. In accretion discs the radial velocity is usually many orders of magnitude smaller than the azimuthal velocity. In our case the Reynolds numbers calculated using the two velocities differ by about five orders of magnitude, if one takes the Keplerian velocity as the characteristic  $\phi$  velocity. For our present calculations only the radial motion is relevant, since  $v_\theta = 0$  in the disc and is proportional to  $v_r$  in the corona, while  $v_\phi$  does not appear in the equation that we are solving now. The value of  $R_m$  reported in figures 2 and 3 is therefore the one calculated taking the characteristic velocity to be the radial velocity. This is a key point for the present considerations: the relevant magnetic Reynolds number is that calculated with the radial velocity and not that calculated with the azimuthal velocity (which gives a much larger value).

The panels in these figures are clearly showing that the distortion of the field is proportional to the magnetic Reynolds number calculated in this way. This happens because with increasing  $R_m$  the freezing condition gets progressively stronger so that any

fluid motion perpendicular to the magnetic field lines encounters more and more resistance. Therefore, since the velocity field is fixed, the magnetic field has to change. Figures 2 and 3 not only show that modifications in the magnetic field lines increase with  $R_m$ , but also that their shape is consistent with what is expected from considering the flux freezing condition in the case of a conical flow (which is what we have in the disc).

However the actual value of the magnetic Reynolds number is somewhat arbitrary, because in general there is no unambiguous way of defining the characteristic length, velocity and diffusivity of a given system. In our case we choose  $l_0$  to be the radius of the inner edge of the disc,  $v_0$  to be the radial velocity at the inner edge of the disc and  $\eta_0$  to be the value of the diffusivity in the main disc region. One could also make a different choice for the characteristic length  $l_0$ , such as taking this to be the radius of the star or the average height of the disc; the trend of having larger distortions for larger values of  $R_m$  would of course be seen in all cases, but the switching on of the distortions would occur at different threshold values of  $R_m$ .

We have already noted that the distortion varies with position, and so it is clear that a single global parameter cannot give a sufficiently detailed description in all parts of the system. It is therefore convenient to introduce a new quantity which we call the “magnetic distortion function”  $D_m$ . We define this in the same way as the magnetic Reynolds number but, instead of taking characteristic values for the velocity and diffusivity, we take the local values:

$$D_m(r, \theta) = \frac{l_0 \cdot |\mathbf{v}(r, \theta)|}{\eta(r, \theta)} \quad (26)$$

This function gives the relative importance of the two terms on the right-hand side of the induction equation at every point of the disc, rather than giving just a global measure as with the standard magnetic Reynolds number. We then expect the advection term ( $\nabla \times (\mathbf{v} \times \mathbf{B})$ ) to dominate in the regions where  $D_m > 1$  and the diffusion term ( $\nabla \times (\eta \nabla \times \mathbf{B})$ ) to dominate when  $D_m < 1$ . This then explains why we find three regions inside the disc: the inner region corresponds to the zone where  $D_m \ll 1$ , the main region to  $D_m \gg 1$ , and the transition region to intermediate values of  $D_m$ . This correspondence is made clear in figure 4, where we show the  $\theta$  component of the magnetic field, the dipolar profile and the magnetic distortion function. We recall that the jump in  $D_m$  follows from the profile chosen for  $\eta$ , i.e. we use a larger value of the diffusivity in the inner part of the disc.

Another important aspect of the magnetic distortion function is that the degree of arbitrariness in its definition is smaller than for the standard magnetic Reynolds number, since it is defined using only one characteristic value,  $l_0$ . In addition there is a quite natural way for choosing  $l_0$ . By looking at equation (25) one can see that, if  $l_0 = r_g$ , the magnetic distortion function is already there in the equation (it is the coefficient of the partial derivative of  $\mathcal{S}$  with respect to  $x$ ). The value  $r_g$  is coming from the way in which we are scaling the lengths. If we had chosen a different unit for the lengths, say  $\tilde{r}$ , then we would have had to choose  $l_0 = \tilde{r}$  if we wanted  $D_m$  to appear directly in equation (25). We can then think of  $l_0$  as a quantity needed to make the ratio  $v/\eta$  dimensionless, and the most natural choice for this is the characteristic scale being used as the unit length.

Summarizing, we can describe the magnetic field configuration in the accretion disc by saying that magnetic field lines that enter the disc in the main region ( $D_m \gg 1$ ) are pushed towards the central object, whereas those which enter the disc in the inner region ( $D_m \ll 1$ ) are almost unmodified. The result is that in between these two regions there is an accumulation of field

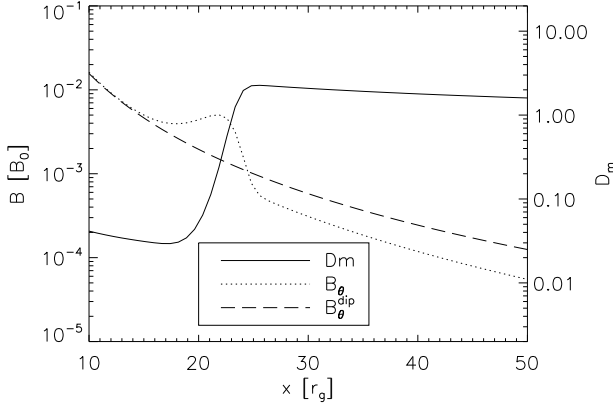


**Fig. 4.** The magnetic field  $B_\theta$  as obtained from the numerical simulations for the configuration with  $R_m = 40$  (dotted) compared with those for a perfect dipolar field (dashed) at the equatorial plane. The solid line is the magnetic distortion function. The scale for  $D_m$  is shown on the right vertical axis. The magnetic field is measured in units of the stellar field,  $B_0 = 3 \cdot 10^8$  G, as shown on the left vertical axis.

lines, and so there is an amplification of the magnetic field there, as can be seen in figure 4.

In order to test the sensitivity of the results to the boundary conditions, we have experimented with several different profiles of the magnetic stream function outside the disc. We have used three additional profiles: one which gives a magnetic field with spherical field lines, one which gives a magnetic field with vertical field lines and another one which gives field lines inclined at an arbitrary angle to the vertical axis. We have chosen these magnetic field profiles by comparison with the results from the simulations by Miller & Stone (1997). For magnetic field lines entering the disc at the same locations, their shape within the disc varies hardly at all in the different cases, although the field intensity does vary significantly. However, we are focusing here on the shape, looking at the distortion of the field lines, which does not depend sensitively on the boundary conditions used and is instead mainly governed by the magnetic distortion function  $D_m$ .

In order to understand better the influence of the magnetic distortion function on the magnetic field structure, we varied  $D_m$  and saw how the field changed. We used three new profiles for  $D_m$  different from the previous one which we then considered as a reference. In the first profile we increased the value of  $D_m$  in the inner part of the disc and left the rest unmodified, in the second one instead we lowered  $D_m$  in the main region of the disc and did not change the inner part, and in the last one we just changed the width of the transition between the low and high values of  $D_m$ . We then calculated the poloidal magnetic field and the results are presented in figure 5, where the top panel shows the different profiles of the magnetic distortion function and the bottom one shows the  $\theta$  component of the magnetic field, referring to the equatorial plane in both cases.

Considering this figure, we can summarize the influence of the magnetic distortion function with four comments: (1) changing the value of  $D_m$  in the small inner part by a factor of 5 leaves the magnetic field almost unchanged, (2) on the other hand, the magnetic field is very sensitive to the width of the transition in  $D_m$  and to its value in the main region, in particular (3) the po-

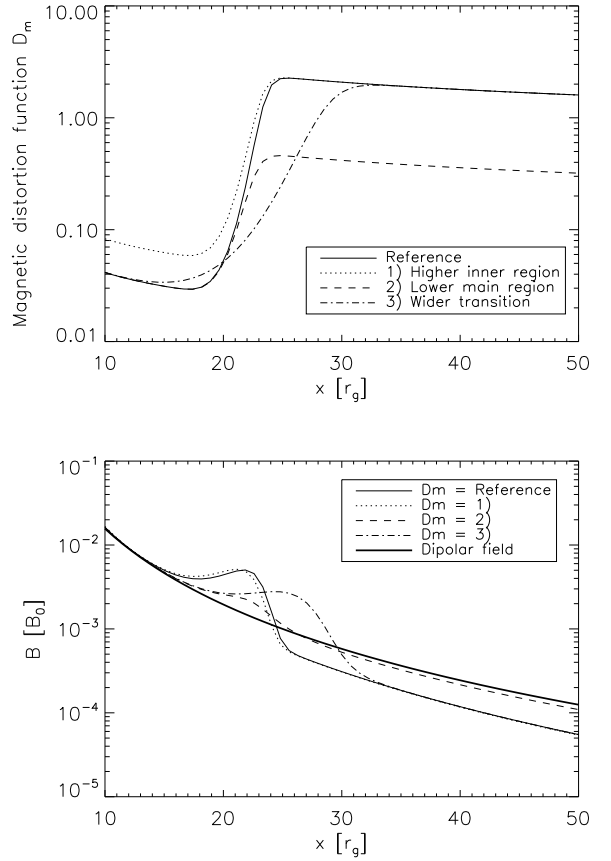


**Fig. 5.** Top panel: magnetic distortion function in the equatorial plane. Bottom panel:  $\theta$  component of the magnetic field in the equatorial plane. For both panels: the solid line shows results from the previous analysis (in the bottom panel the dipolar field is shown with a thick solid line); the dotted lines refer to profile 1 (larger value of  $D_m$  in the inner region only); the dashed lines refer to profile 2 (lower value of  $D_m$  in the main region only); the dot-dashed lines refer to profile 3 (same values of  $D_m$  in inner and main region, but the transition region is wider).

sition of the peak in  $B_\theta$  is related to the width of the transition and (4) the deviations away from the dipole field are mainly governed by the value of  $D_m$  in the main region. We can go further and consider the radial derivative of  $D_m$ , which is shown in figure 6 for all of the profiles used. From this we can see that the position of the peak of  $B_\theta$  is strongly connected with the position of the minimum in  $\partial_r D_m$ , and that the maximum amount of magnetic distortion is related to the depth of the dip in the derivative of  $D_m$ .

Finally we comment on the behaviour of the magnetic stream function in the equatorial plane. In order for the magnetic field to have a local minimum or maximum, its first radial derivative must, of course, be zero. This condition can be written in terms of  $S$  as:

$$\partial_r^2 S - \frac{1}{r} \partial_r S = 0 \quad (27)$$

In the numerical simulations  $S$  is always decreasing with  $r$  and so the only way to get a local minimum or maximum is for  $S$  to go through a region where its concavity is reversed and becomes negative. An example of this is shown in figure 7, where we plot



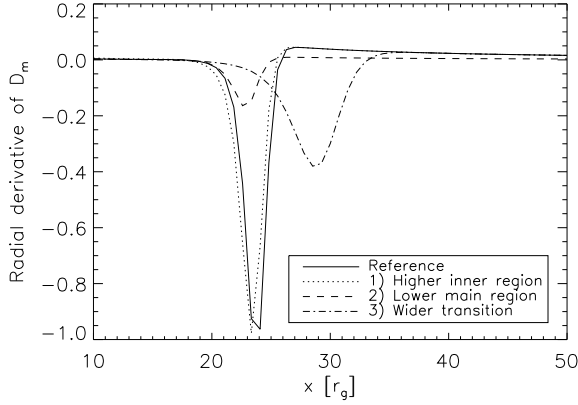


**Fig. 6.** Radial derivative of the magnetic distortion function in the equatorial plane. The profiles refer to the same case as in figure 5. Comparing with the bottom panel of figure 5 one can see that the peaks in the magnetic field  $B_\theta$  occur at almost the same locations as where  $\partial_r D_m$  has a minimum, and that the amplitudes of the distortions are proportional to the absolute values of the minimum of  $\partial_r D_m$ .

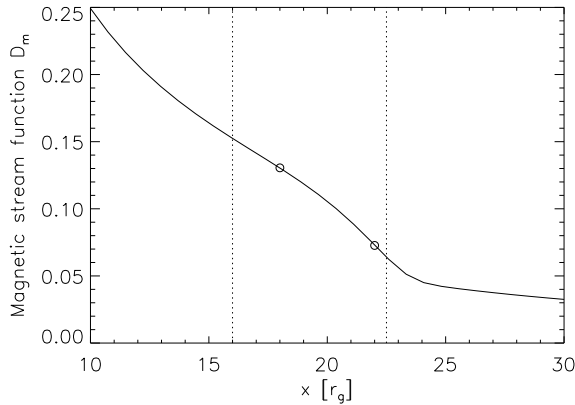


**Fig. 7.** The magnetic stream function  $S$  for the reference profile. The dotted lines are drawn where  $S$  changes concavity, while the open circles mark the locations where  $B_\theta$  has a minimum or a maximum, i.e.  $r \sim 18 r_g$  and  $r \sim 22 r_g$ ; they are in the region where the concavity of the magnetic stream function is negative.

the stream function for the reference case. We can see that for  $r < 16 r_g$  and  $r > 22.5 r_g$   $S$  has positive concavity, while between these two values it is negative. The dotted lines in the figure delimit the regions of positive and negative concavity, while the open circles are drawn at the locations where  $B_\theta$  has a minimum or a maximum. As expected these points are in the region of negative concavity.

## 5. Conclusions

In this paper we have begun a systematic study of the magnetic field configuration inside accretion discs around magnetised neutron stars, which is intended as being complementary to the large numerical simulations being carried out elsewhere. We have assumed that the star itself has a dipolar magnetic field,

that is rotating around its magnetic axis and that this axis is perpendicular to the disc plane. We have also assumed that the flow is steady and has axial symmetry everywhere. Our strategy was to start the analysis with a very simple model, where we made the kinematic approximation and solved the induction equation numerically in full 2D, without making any leading order expansion. This initial model will subsequently be improved by including the magnetic backreaction on the fluid flow.

We have shown that it is possible to separate the calculation for the configuration of the poloidal magnetic field from any azimuthal quantities. This is a key point and has the consequence that the effective magnetic Reynolds number is that calculated with the radial velocity rather than the azimuthal one (which is very much larger). We have here considered only the poloidal component; the toroidal one will be addressed in a subsequent paper.

We have modelled the system as being composed of four regions (see figure 1): the central neutron star, the disc, the corona (taken to be a layer above and below the disc) and all of the rest, which is taken to be vacuum. We suppose that the stellar magnetic field remains dipolar until it reaches the corona. At that point it begins to feel the presence of the fluid flow and the magnetic field lines are pushed inwards, thus creating distortions away from the purely dipolar field.

We have studied the response of the magnetic field to changes in the velocity and the diffusivity, finding distortions away from dipolar increasing with the radial infall velocity and decreasing with increasing diffusivity. The underlying behaviour is that the distortions increase together with the magnetic Reynolds number  $R_m$  (which governs the flux freezing condition) where the ratio  $v_0/\eta_0$  appears.

However a single value of  $R_m$  cannot take into account any large changes in the magnitudes of the velocity and the diffusivity through the disc, since it is defined using single characteristic values. Therefore in order to have a sufficiently detailed description of the system, we have introduced a magnetic distortion function  $D_m = \frac{l_\theta \cdot |\mathbf{v}(r, \theta)|}{\eta(r, \theta)}$ , based on local values of the quantities concerned, so that in the regions where  $D_m \gg 1$  or  $D_m \ll 1$  one should expect to have large or small distortions respectively. We expect the turbulence to be enhanced in the regions of lower density (the corona and the inner part of the disc), therefore in our model we use a larger value of  $\eta$  in these regions, giving a smaller value for  $D_m$ . As clearly shown in the panels of figures 2 and 3, the disc can be divided into three parts: (1) an inner region, where  $D_m \ll 1$  and the distortions are negligible; (2) a transition region, where  $D_m$  is rapidly increasing and magnetic field lines accumulate; (3) a main region, where  $D_m \gg 1$  and the distortions are very large. Considering  $D_m$  can be very useful when analysing results of large numerical simulations.

Comparing our results with previous literature, we can confirm the idea of dividing the disc into two principle regions: an inner part, where the magnetic field is strongest, and an outer part, where the magnetic field is weaker and gently decaying. However the behaviour that we find for the field in these regions is very different from that of the Ghosh & Lamb model (1979a) and we find it convenient to include a third zone, to be considered as a transition between the two principle ones (see figure 4). In the inner boundary layer of the GL model, the magnetic field is reduced by screening currents by a factor of 80 per cent, while in our case the field is barely modified in the first region. In the transition region instead we see a completely new effect: the field is amplified and has a local maximum. The properties of the maximum (i.e. its location, the peak magnitude of the field and

its behaviour in the neighbourhood) are well described by the magnetic distortion function  $D_m$ , in particular by its maximum value, by the width of the transition between the low and high value and by the behaviour of the radial derivative  $\partial_r D_m$  (i.e. by the location and the magnitude of its minimum). The behaviour in the outer zone is instead quite similar to that in the GL model, with the field decaying and being smaller than the dipole one at any give location.

As regards the magnetic field geometry, our results resemble rather closely those obtained by Miller & Stone (1997) (compare our figure 3 with the top panels of their figure 3), despite the fact that they solved the full set of MHD equations whereas we have solved just the induction equation and with different conditions at the top of the disc. Moreover we have found that the distortion of the field lines inside the disc depends very little on the profiles outside it. We conclude that the distortion pattern seen for the poloidal component of the magnetic field should be rather a general result, related only to the fundamental aspects of the system, and that the distortion is not at all negligible for typical values of the accretion rate (see figures 2 and 3).

The immediate next step will be that of calculating the toroidal magnetic field component, by solving equation (7), and consequently the magnetic torque. After that we will move to the next model, by removing the kinematic approximation and solving the Euler equation as well as the induction equation. By comparing the results of that calculation with those for the present kinematic model, we will be able to understand the effects of the magnetic backreaction, which we expect to affect mainly the toroidal magnetic field component.

## Acknowledgments

It is a pleasure to thank Alfio Bonanno, Claudio Cremaschini and Kostas Glampedakis for stimulating discussions; this work was partly supported by CompStar, a Research Networking Programme of the European Science Foundation.

## References

- Abbott B. et al., 2007, Phys.Rev.D, 76, 042001  
 Agapitou V. & Papaloizou J.C.B. 2000, MNRAS, 317, 273  
 Balbus S.A. & Hawley J.F. 1991, ApJ, 376, 214  
 Bildsten L., Chakrabarty D., Chiu J. et al. 1997, ApJS, 113, 367  
 Bonanno A. & Urpin V. 2006, Phys. Rev. E, 73, 066301  
 Bonanno A. & Urpin V. 2007, ApJ, 376, 214  
 Campbell C.G. 1987, MNRAS, 229, 405  
 Campbell C.G. 1992, GApFD, 63, 179  
 Chandrasekhar S. 1960, Proc. Natl. Acad. Sci., 46, 253  
 Davidson K. & Ostriker J. P. 1973, ApJ, 179, 585  
 Elstner D. & Rüdiger G. 2000, A&A, 358, 612  
 Ghosh P., Lamb F.K. & Pethick C.J. 1977, ApJ, 217, 578  
 Ghosh P. & Lamb F.K. 1979a, ApJ, 232, 259  
 Ghosh P. & Lamb F.K. 1979b, ApJ, 234, 296  
 Illarionov A. F. & Sunyaev R. A. 1975, Astr. Ap., 39, 185  
 Kiziltan B. & Thorsett S.E. 2009, ApJ, 693, L109  
 Kluzniak W. & Rappaport S. 2007, ApJ, 671, 1990  
 Kulkarni A. K. & Romanova M. M. 2008, MNRAS, 386, 673  
 Mestel L. 1961, MNRAS, 122, 473  
 Miller K. A. & Stone J. M. 1997, 489, 890  
 Romanova M. M., Ustyugova G. V., Koldoba A. V. & Lovelace R. V. E. 2002, ApJ, 578, 420  
 Rüdiger G., Hollerbach R., Schultz M. & Elstner D. 2007, MNRAS, 377, 1481  
 Rüdiger G. & Shalibkov D. 2002, A&A, 393, L81  
 Shakura N.I. 1975, Soviet Astr. Letters, 1, 223  
 Shakura N.I. & Sunyaev R.A. 1973, A&A, 24, 337  
 Shalibkov D. & Rüdiger G. 2000, MNRAS, 315, 762  
 Tayler R.J. 1973, MNRAS, 161, 365  
 Turner N.J. Sano T., 2008 ApJ, 679, L131  
 Velikov E.P. 1959, Sov. Phys. JETP, 9, 995

Wang Y.-M. 1987, A&A, 183, 257

## Appendix A: The Code

In this Appendix we describe the computer code that we have used to solve equation (25) and discuss some of the tests that we have performed to verify it.

### A.1. Description of the code

In order to solve the 2-D elliptic PDE (25) we use the Gauss-Seidel relaxation method. If we call the elliptic operator  $\mathcal{L}$  and the right hand side  $b$ , then the original equation becomes:  $\mathcal{L}[S] = b$ . We turn this elliptic equation into a hyperbolic one by adding a pseudo time derivative; we can then consider the iterative procedure as a time evolution and write:  $\partial_t S = \mathcal{L}[S] - b$ . In our case  $\mathcal{L} = \partial_x^2 + \frac{1}{x^2} \partial_y^2 - \left( \frac{\cot y}{x^2} + \frac{v_\theta r_g}{x\eta} \right) \partial_y - \frac{v_r r_g}{\eta} \partial_x$  and  $b = 0$ .

We then approximate the operators by discretizing the functions over a grid. The scheme that we use for discretizing the derivatives is as follows:

$$\partial_\theta S|_{i,j} = \frac{S_{i,j+1} - S_{i,j-1}}{2\Delta j} \quad \text{and} \quad \partial_\theta^2 S|_{i,j} = \frac{S_{i,j+1} - 2S_{i,j} + S_{i,j-1}}{\Delta j^2} \quad (\text{A.1})$$

$$\partial_r S|_{i,j} = \frac{S_{i+1,j} - S_{i-1,j}}{2\Delta i} \quad \text{and} \quad \partial_r^2 S|_{i,j} = \frac{S_{i+1,j} - 2S_{i,j} + S_{i-1,j}}{\Delta i^2} \quad (\text{A.2})$$

$$\partial_t S = \frac{S^{t+1} - S^t}{\Delta t} \quad (\text{A.3})$$

where the indices  $i$  and  $j$  refer to grid points along the  $x$  and  $y$  coordinate directions respectively, while  $t$  represents the pseudo-time or iteration step. We use expressions (A.1)-(A.3) to discretize equation (25) and then, isolating the term  $S_{i,j}^{t+1}$ , we get the iterative algorithm that we use in our code:

$$S_{i,j}^{t+1} = S_{i,j}^t + \Delta t \left[ \frac{S_{i+1,j}^t - 2S_{i,j}^t + S_{i-1,j}^{t+1}}{\Delta i^2} + \frac{1}{x_i^2} \frac{S_{i,j+1}^t - 2S_{i,j}^t + S_{i,j-1}^{t+1}}{\Delta j^2} + \left( \frac{\cot y_j}{x_i^2} + \frac{v_\theta r_g}{x_i \eta} \right) \frac{S_{i,j+1}^t - S_{i,j-1}^{t+1}}{2\Delta j} - \frac{v_r r_g}{\eta} \frac{S_{i+1,j}^t - S_{i-1,j}^{t+1}}{2\Delta i} \right] \quad (\text{A.4})$$

We solve this proceeding outwards from  $i = 1, j = 1$ ; on the right hand side the terms that have already been calculated (i.e. the terms at positions  $i = i - 1$  and  $j = j - 1$ ) are taken at the current iteration  $t + 1$ , as usual in the Gauss-Seidel method. We provide an initial estimate for  $S$  at iteration zero and the code then modifies this by relaxing the solution using the chosen profiles of  $v_r, v_\theta$  and  $\eta$ , which are all functions of  $r$  and  $\theta$ .

The magnitude of the central dipole field and the accretion rate do not enter this equation directly, but they are used to calculate the inner edge of the disc  $r_{in}$ . We recall that we have a radial numerical domain going from  $r_{in}$  to  $r_{out}$ , and a physical domain of interest which begins at the same radius but stops earlier, at the light cylinder radius  $r_{lc}$ . Along the  $\theta$  direction the two domains coincide and go from  $\theta_{top}$ , which is the top surface of the corona, to  $\theta_{eq}$ , which is the equatorial plane (because of the

symmetry of the system with respect to the equatorial plane, the solution below the equator will be the same as above it).

For the mass and radius of the neutron star, we use the canonical values,  $1.4 M_\odot$  and 10 km respectively. We fix the accretion rate as  $\dot{m} = 0.03$  (in units of  $\dot{M}_{\text{Edd}}$ ), giving a magnetospheric radius of about  $10 r_g$  when  $B_0 \sim 3 \cdot 10^8$  G, as typical for a millisecond pulsar.

## A.2. Testing of the code

In order to check the code for stability and convergence, to estimate errors and to optimize the iteration procedure by choosing an appropriate iteration step, we performed a number of tests, some of which are now described.

During this test phase we used the following values for the parameters:

- magnetic field at the stellar surface:  $B_0 = 3 \cdot 10^8$  G;
- size of the domain:  $r_{\text{in}} = 10 r_g$ ,  $r_{\text{out}} = 750 r_g$ ,  $\theta_{\text{top}} = 80^\circ$ ,  $\theta_{\text{eq}} = 90^\circ$  and  $\theta_c = 82^\circ$ ;
- radial velocity at inner edge:  $v_r(r_{\text{in}}) = v_0 = 10^5 \text{ cm s}^{-1}$  which is the value obtained from equation (11) when  $(\alpha, \dot{m}) = (0.15, 0.03)$  or  $(0.1, 0.07)$ ;
- diffusivity:  $r_{\eta \text{ in}} = r_{\text{in}}$ ,  $r_{\eta \text{ out}} = r_{\text{out}}$ ,  $\eta_0 = 10^{10} \text{ cm}^2 \text{ s}^{-1}$  and  $\eta_c = 10^{12} \text{ cm}^2 \text{ s}^{-1}$ ;
- initial estimate for the magnetic stream function:  
 $S = r_0 \cdot \sin \theta / r^{0.5}$  (for a dipolar field  $S^{\text{dip}} = r_0 \sin^2 \theta / r$ );
- iteration time step:  $\Delta t = 3 \cdot 10^{-2} \cdot \Delta x \cdot \Delta y$ .

The tests can be divided into two main groups: with and without a known analytic solution. For the latter, we can estimate errors by calculating the residuals and comparing the solutions obtained with different grid resolutions, while for the former we also have the difference between the computed values and the exact results.

### A.2.1. Test with an analytic solution

There are two cases for which we can obtain an analytic solution. The first has dipolar boundary conditions and no poloidal motion ( $v_r = v_\theta = 0$ ); in this case the poloidal component of the field must be dipolar everywhere (we refer to this test as D, for dipolar). In Section 3 we showed that, in order to have a dipolar field as a stationary solution of the induction equation, the poloidal velocity has to fulfill the relation given by equation (21) and using  $v_r = v_\theta = 0$  is consistent with that condition. Our second analytic test case has the boundary conditions for  $S$  set to zero. In this case, regardless of the profile used for the velocity,  $S(r, \theta) = 0$  is a solution in all of the domain (we call this test Z, for zero). Even if at first glance a test with an identically zero solution may seem to be of little importance, we think that it is useful, because in this way we can test the code by including all of the terms that will be present when solving for the cases of interest (i.e. including  $v_r$ ,  $v_\theta$  and  $\eta$ ).

In both cases, we test two different configurations by changing the velocity profile. In test D we consider a case with zero velocity (test D1) and another one where  $v_\theta$  is given by equation (21) and with  $v_r$  given by equation (11) in the corona and being zero in the disc (test D2). In test Z we consider the same velocity profile as the one that we will use for our cases of interest, given by equations (11) and (21) (test Z1), and a velocity profile which is the same as that used in test D2 (test Z2).

In all of these tests we follow the same procedure, we verify the stability of the code, we estimate the error and see if it

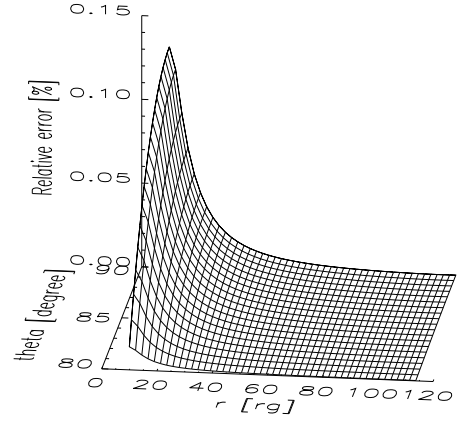


**Fig. A.1.** Relative error at each grid point of the region of interest for a representative case: test D2 with a  $400 \times 20$  grid. For the other grids (and tests) the results have exactly the same qualitative behaviour, but the precise value of the error is different and increases if the number of grid-points is decreased. For the  $100 \times 20$  grid, the maximum relative error is  $\sim 15$  per cent, while for the  $200 \times 20$  grid it is about 0.8 per cent and finally for the  $400 \times 20$  grid (shown in the figure) it is 0.15 per cent.

scales correctly, checking the convergence of the solution. We do this by studying how the numerical solution changes when varying the number of grid points ( $N_i$  and  $N_j$ ) and the number of iterations.

We use five grids in total. When testing the dependence on  $N_j$  we use:  $200 \times 20$ ,  $200 \times 40$  and  $200 \times 80$ ; while when testing the dependence on  $N_i$  we use:  $100 \times 20$ ,  $200 \times 20$  and  $400 \times 20$ . For each of these grids we calculate: (i) the absolute difference and (ii) the relative difference, between the numerical solution and the analytic one at each point of the grid; and (iii) the root mean square (rms) of the numerical solution  $S$  at each iteration step. The results obtained are very similar for all of the five grids and for each of the four tests and can be summarized with the following four statements: (1) both the absolute error and the relative error have a maximum near to the inner edge  $r_{\text{in}}$  and then decrease quite rapidly. With the  $400 \times 20$  grid, the maximum relative error is about 0.1 per cent (see fig. A.1); (2) changing  $N_j$  does not produce any visible effect: while increasing  $N_j$  by a factor of 4 (from 20 to 80) decreases the maximum relative error only slightly ( $\sim 7$  per cent), changing  $N_i$  from 100 to 400 has a much greater effect, giving a decrease in the error of two orders of magnitude; (3) the reduction in the rms and in the maximum error becomes progressively smaller with increasing  $N_i$ , thus showing that we have convergence of the numerical solution; (4) using a sparser grid gives smaller errors at the beginning and during the relaxation process, however if one keeps iterating until the saturation level is reached, then the error with sparser grids is larger than with denser grids (suggesting that this problem could be suited for a multigrid approach). Regarding statements (2), (3) and (4), see fig. A.2.

### A.2.2. Test with an unknown solution

We use now a configuration with dipolar boundary conditions and a velocity field given by equations (11) and (21). This is very similar to test D2, but in this configuration  $v_r$  is not taken to be zero in the disc. Even if we do not know the solution for

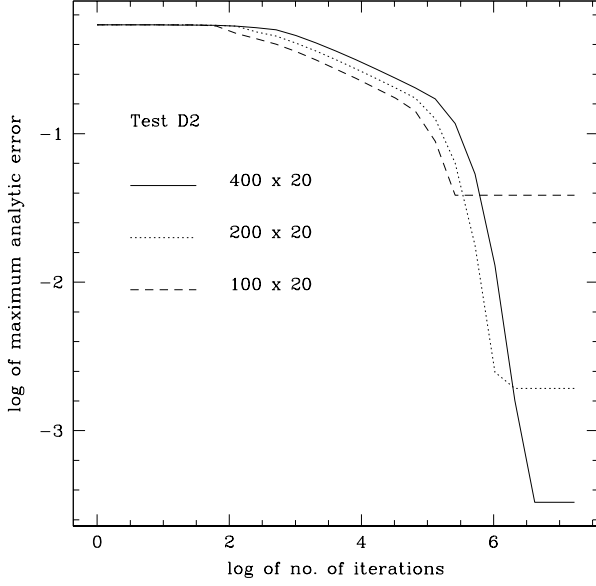


**Fig. A.2.** Maximum analytic error for the test D2 with three grids, which differ only in  $N_i$ . Increasing  $N_j$  from 20 to 80 produces a very small decrease in the error, only  $\sim 7\%$ .

this setup, we know from equation (10) that it has to approach a dipolar field when the coefficients  $\frac{v_\theta}{r\eta}$  and  $\frac{v_r}{r\eta}$  both go to zero. In order to test this we have considered five configurations, each with a different value of  $\eta_0$  ranging between  $10^{11}$  and  $10^{15} \text{ cm}^2 \text{ s}^{-1}$  ( $\eta_c$  is always taken to be two orders of magnitude larger than  $\eta_0$ ). Figure A.3 shows clearly that for increasing  $\eta$ , the rms of the numerical solution is approaching that for a dipole calculated on the same grid.

For these five configurations we also performed the tests previously described, i.e. the ones regarding changing the grid and comparing the errors and the rms. The results are again similar and confirm the four statements made earlier.

### A.2.3. Other tests

We next used the configuration of test D2 for checking three more aspects: determining the importance of the initial estimate for  $S$  and investigating which values to choose for the location of the outer radial boundary and for the iteration step.

The kind of algorithm which we are using to solve equation (10) needs an initial estimate for the solution. According to how good or bad this estimate is with respect to the correct solution, one needs a smaller or larger number of iterations for completing the process. In order to show this and also to demonstrate that the final solution does not depend on the initial profile, we used four initial estimates for the magnetic stream function  $S$ : (1) a constant value, (2) a Gaussian profile (centred on  $r = 100 r_g$  and with a width of  $20 r_g$ ), (3) a profile increasing with  $r^3$  (this gives  $B_r$  and  $B_\theta$  increasing linearly with  $r$ ) and (4) the profile which gives a dipolar magnetic field (the analytic solution for this configuration is  $S = r_0 \cdot \sin \theta / r^{0.5}$ ). In all of the cases the final solution is the same, even for configuration (3), but the number of iterations required to reach saturation changes and goes from 0 for case (4) to  $2^{20}$  for cases (1) and (2) and to  $2^{26}$  for case (3).

As mentioned previously (in Sections 2 and A.1), our region of physical interest goes from the inner edge of the disc  $r_{in}$  out

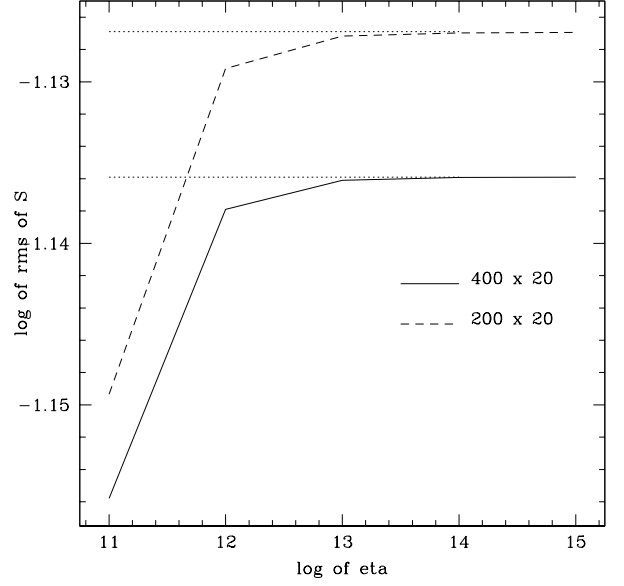


**Fig. A.3.** The rms of the numerical solution for different values of  $\eta$  after  $2^{24}$  iterations. When  $\eta \rightarrow \infty$ , the rms should reach the value for a dipole, which is plotted with a dotted line for both grids.

to the light cylinder  $r_{lc}$ . Since we do not want the solution in this region to be influenced by the outer boundary condition, we ran some tests using different values for the radius of the outer edge  $r_{out}$  and then compared the numerical solutions in the region of interest. We used the same setup as for the real problem that we were wanting to solve, i.e. with dipolar boundary conditions, the velocity field given by equations (11) and (21) and the diffusivity given by equation (16). We used six values of  $r_{out}$  ( $150 r_g$ ,  $200 r_g$ ,  $250 r_g$ ,  $300 r_g$ ,  $500 r_g$  and  $750 r_g$ ) and we found that the difference within the region of interest between the numerical solutions obtained using two subsequent values of  $r_{out}$  became progressively smaller, until one could barely distinguish the different solutions. We decided to put the outer boundary at  $750 r_g$  for the physical analysis; this gives results differing from those with  $r_{out} = 500 r_g$  by less than about 5 per cent.

Finally we considered varying the iteration step size, i.e. the  $\Delta t$  in equation (A.4), that is written as  $c \cdot \Delta r \cdot \Delta \theta$ . There is no simple argument of principle that can be used to determine the best value for  $c$ , therefore we determined it experimentally. We considered the same configuration as in test D2 and ran it several times varying only the value of  $c$ , going from 0.025 upwards. We found that the final asymptotic error was always the same, but that the number of iterations required to relax to the final solution was changing, decreasing as  $c$  increased. However there is an upper limit: when  $c > c_{max} = 1.25$  the numerical solution diverges. Transferring this condition to  $\Delta t$ , we obtain  $\Delta t_{max} = 8.5 \cdot 10^{-3}$ . We can then change the way in which the iteration step size is calculated in the code and write:  $\Delta t = n \cdot \Delta t_{max}$ , with  $n$  always smaller than 1. We find that using the value  $n = 0.95$  is a good compromise in minimizing the number of iterations and preserving the code stability.